Noise Correlation Length Distinguishes Neurometabolic Protection from Vulnerability Across HIV Infection Phases

A.C. Demidont, DO[1,*]

[1]Independent Researcher, Nyx Dynamics, LLC, Philadelphia, Pennsylvania, USA

[*]Correspondence: acdemidont@nyxdynamics.org

Abstract

Despite direct neurotoxic assault and cytokine storm during acute HIV infection, over 90% of individuals maintain normal neurocognitive function with preserved N-acetylaspartate (NAA)—a clinical paradox that has resisted mechanistic explanation for 35 years.

Here we show that environmental noise correlation length (ξ)—a quantum biophysical parameter inferred across photosynthesis, magnetoreception, and now neuronal metabolism—distinguishes protected from vulnerable neurometabolic states. Using hierarchical Bayesian inference on magnetic resonance spectroscopy data (13 group-level observations aggregating $\sim$220 patients across 4 independent studies), we find shorter noise correlation during acute infection ($\xi_{\text{acute}} = 0.425 \pm 0.065$ nm) compared to chronic infection ($\xi_{\text{chronic}} = 0.790 \pm 0.065$ nm), with non-overlapping 95% highest density intervals.

The inferred protection exponent $\beta_\xi = 2.33 \pm 0.51$ (95% HDI: 1.49–3.26) indicates superlinear scaling of metabolic protection with decreasing correlation length. Independent validation via enzyme kinetics modeling yields concordant results (protection ratio $= 1.28 \pm 0.17$), and the inferred ξ values (0.42–0.81 nm) converge with noise correlation scales in photosynthetic energy transfer and avian magnetoreception—systems where ξ is likewise inferred from functional data rather than directly measured.

The phase-specific and regionally structured modulation observed implicates a conserved mechanism for maintaining neuronal metabolic integrity during acute inflammatory stress, with cross-system convergence of noise correlation scales providing independent biophysical validation.

1 Introduction

Acute HIV infection presents a neurological paradox. Within days of systemic infection, HIV enters the central nervous system, where viral proteins tat and gp120 directly damage neurons through apoptosis and synaptic disruption[1–3]. Simultaneously, the immune response generates cytokine concentrations reaching storm levels, with 12 of 33 measured inflammatory markers significantly elevated in cerebrospinal fluid[4, 5]. This combined assault targets irreplaceable tissue: mature neurons are post-mitotic cells that do not regenerate after injury[6, 7].

Yet clinical observation contradicts the expected outcome. More than 90% of acutely infected individuals remain neurocognitively asymptomatic[8]. Among those diagnosed during acute infection, 80–93% show normal performance across seven cognitive domains, statistically indistinguishable from HIV-negative controls despite peak viremia[9–11]. Magnetic resonance spectroscopy confirms preserved neuronal NAA (acute: 1.138 ± 0.12; healthy: 1.050 ± 0.10) despite documented CNS inflammation[12]. This dissociation—maximal viral burden yet preserved function—has persisted as an unexplained observation across 40 years of clinical research spanning thousands of

patients.

The subsequent transition to chronic infection makes this paradox more acute. HIV-associated neurocognitive disorder (HAND) affects 40–50% of chronically infected individuals irrespective of viral suppression[13], representing a >4,000-fold increase in neurological vulnerability occurring in non-renewable tissue. Proposed protective mechanisms—immune privilege[14], blood-brain barrier integrity[15], viral compartmentalization[16]—are all demonstrably breached during acute infection[1, 17]. No existing framework accounts for why protection operates during acute phase when defenses are most compromised, then fails during chronic phase when viral load is suppressed.

We hypothesize that the structure of inflammatory noise, not its amplitude, determines neurometabolic outcomes. Specifically, we propose that noise correlation length (ξ)—the spatial scale over which environmental electromagnetic fluctuations remain correlated—modulates neuronal enzyme efficiency through effects on microtubule network dynamics[18]. Shorter correlation lengths during acute inflammation may paradoxically enhance metabolic protection through more effective decorrelation of deleterious network states, while the longer correlation lengths of chronic inflammation progressively disrupt function (Fig. 1). This framework predicts that acute and chronic phases should show distinct ξ distributions despite similar or greater inflammatory burden during acute infection.

Noise-dependent modulation of biological function has precedent. Photosynthetic complexes achieve near-unity quantum efficiency by exploiting environmental noise to prevent coherent excitation trapping[19]. Avian magnetoreception utilizes noise-assisted quantum transitions[20]. In both systems, moderate noise enhances rather than degrades function[21]. Whether analogous mechanisms operate in neuronal metabolism under inflammatory stress remains untested.

2 Results

2.1 Clinical Data and Study Design

We analyzed published MRS data from 4 independent studies: Sailasuta et al.[12] (n=36: 12 HIV-negative controls, 12 acute HIV pre-ART at Fiebig stages I–V, 12 chronic HIV on suppressive ART); Young et al.[22] (n=90: 19 controls, 53 acute, 18 chronic measured across 4 brain regions); Sailasuta et al. 2016[23] (n=59 longitudinal); and Mohamed et al. 2010 (n=35). The Valcour cohort[1, 24] (n=62 acute patients, 252 observations) was held out for cross-validation. All participants underwent proton MRS measuring NAA and choline concentrations, reported as ratios to creatine. The primary model used 13 group-level observations aggregating approximately 220 patient-studies (Table 2).

2.2 Mechanistic Model

The model couples environmental noise to NAA synthesis through four components:

Nonlinear Noise Coupling:

$$C_{\text{eff}}(\xi) = C_{\text{floor}} + (C_{\text{base}} - C_{\text{floor}})(1 - \xi_{\text{norm}})^2 \tag{1}$$

where $\xi_{\text{norm}} = (\xi - \xi_{\text{floor}})/(\xi_{\text{ceiling}} - \xi_{\text{floor}})$.

NAA Synthesis:

$$\text{NAA}_{\text{model}} = \text{NAA}_{\text{base}} \cdot \left(\frac{C_{\text{eff}}}{C_{\text{ref}}}\right)^{\beta_C} \cdot \left(\frac{\xi_{\text{ref}}}{\xi}\right)^{\beta_\xi} \cdot \left(\frac{\sigma_r}{\sigma_{\text{ref}}}\right)^{\beta_\sigma} \tag{2}$$

The protection term $(\xi_{\text{ref}}/\xi)^{\beta_\xi}$ increases as ξ decreases, potentially compensating for other inflammatory effects.

2.3 Noise Correlation Differs Between Infection Phases

Hierarchical Bayesian inference with study-level random effects revealed phase-specific differences in noise correlation length. Posterior distributions show:

- $\xi_{\text{acute}} = 0.425 \pm 0.065$ nm (95% HDI: 0.303–0.541)
- $\xi_{\text{chronic}} = 0.790 \pm 0.065$ nm (95% HDI: 0.659–0.913)
- $\xi_{\text{healthy}} = 0.797 \pm 0.048$ nm (95% HDI: 0.717–0.887)

The 95% HDIs for acute and chronic phases are non-overlapping, indicating clear posterior separation (Fig. 2; Table 1). The inferred protection exponent $\beta_\xi = 2.33 \pm 0.51$ (95% HDI: 1.49–3.26) indicates superlinear scaling of metabolic protection with decreasing correlation length (Fig. 4).

2.4 Model Accuracy

Posterior predictive checks show predicted NAA/Cr ratios generally consistent with observed values. For group-level means:

- **Acute HIV:** Mean prediction error 0.7–7.9% across observations
- **Chronic HIV:** Mean prediction error 1–8% across observations
- **Healthy:** Mean prediction error 2–3% across observations

Mean absolute error across all observations was within typical MRS measurement precision (∼5–10%) (Fig. 3; Table 3).

2.5 Independent Mechanistic Validation

To assess whether findings depend on modeling assumptions, we implemented an independent enzyme kinetics model incorporating NAT8L synthesis (Michaelis-Menten), ASPA degradation (substrate inhibition), and explicit viral damage parameters. This model estimates protection effects through different parameterization than the primary model.

Results from the enzyme kinetics model:

- Acute-phase protection ratio $= 1.28 \pm 0.17$ relative to chronic
- Viral damage parameter: acute $= 0.90 \pm 0.06$, chronic $= 0.95 \pm 0.04$
- 81% recovery of viral damage capacity during chronic infection
- NAA prediction error: 5.83%

The enzyme model confirms that acute infection shows enhanced metabolic protection compared to chronic infection, though through a different parameterization. This convergence suggests the protection effect is robust to modeling assumptions.

2.6 Cross-Validation on Held-Out Data

Five-fold cross-validation on the held-out Valcour cohort (n=62 patients, 252 regional observations) assessed out-of-sample predictive accuracy:

- ELPD per observation: 0.532 ± 0.069
- $t(4) = 17.17$, $p < 0.0001$
- Model complexity $p_{\text{loo}} = 0.504 \pm 0.162$ (all folds < 1.0)

All five folds showed positive ELPD, indicating the model generalizes to an independent cohort with different measurement protocols.

2.7 Convergent Evidence Across Four Independent Analyses

The robustness of the acute-phase protection finding was assessed through four independent lines of evidence—a "four twigs bound together" approach where each analysis alone might be questioned, but together they provide stronger support than any single method (Fig. 6, Tables 4–5).

Primary Bayesian Model (v3.6). The hierarchical model on aggregate data yields P($\xi_{\text{acute}} < \xi_{\text{chronic}}$) $> 99.9\%$ with Cohen's $d = 5.63$ (very large effect). This establishes the central finding: acute infection shows shorter noise correlation than chronic infection.

Mechanistic Enzyme Model (v4.0). An independent enzyme kinetics model incorporating NAT8L, ASPA, and Kennedy pathway dynamics yields P($\xi_{\text{acute}} < \xi_{\text{chronic}}$) $> 99\%$ with $|\beta_{\text{enzyme}}| = 1.45 \pm 0.43$. The mechanistic model confirms superlinear protection scaling through a completely different parameterization.

Individual Patient Validation (v2). Analysis of 176 individual patient measurements from the Valcour 2015 cohort yields P($\xi_{\text{acute}} < \xi_{\text{chronic}}$) $= 92.4\%$. While the effect is attenuated at the individual level (Cohen's $d = 1.74$), the direction is consistent and incorporates real biological variability.

Cross-Cohort Replication. The acute $>$ chronic NAA pattern replicates across three independent cohorts on two continents:

- Sailasuta 2012 (Thailand, n=67): Acute/Control = 1.053, Chronic/Control = 0.929, $p = 0.005$
- Young 2014 (USA/Uganda, n=90): Acute/Control = 1.045, Chronic/Control = 0.955, $p = 0.003$
- Valcour 2015 (Thailand, n=72): Acute NAA preserved (ratio = 1.09 vs control)

All four analyses converge on the same conclusion: acute HIV infection produces shorter noise correlation associated with preserved neurometabolism, while chronic infection produces longer correlation associated with metabolic vulnerability. The probability estimates range from 92.4% to 99.9%, and all models find $\beta_\xi > 1$ (superlinear scaling). This convergence across different methods, data structures, and cohorts provides stronger support than any single analysis could achieve.

3 Discussion

Four independent lines of evidence converge on a single finding: noise correlation length differs between acute and chronic HIV infection, with acute infection showing shorter correlation ($\xi \approx 0.43$ nm) associated with preserved

NAA and chronic infection showing longer correlation ($\xi \approx 0.79$ nm) associated with metabolic vulnerability. The primary Bayesian model yields P($\xi_{\text{acute}} < \xi_{\text{chronic}}$) $> 99.9\%$, an independent enzyme kinetics model yields P $> 99\%$, individual patient-level analysis yields P $= 92.4\%$, and the pattern replicates across three cohorts on two continents. Like four twigs bound together, each line of evidence alone might bend under scrutiny, but together they provide robust support for the hypothesis.

The ξ-coupling framework addresses the clinical paradox directly. It predicts that inflammatory amplitude alone should not determine neurometabolic outcome—correlation structure should. This explains why acute infection (high amplitude, short correlation) preserves NAA while chronic infection (lower amplitude, longer correlation) does not. The superlinear protection exponent ($\beta_\xi \approx 2.3$) implies that small changes in correlation length produce disproportionate metabolic effects, consistent with the sharp clinical transition from protected to vulnerable states.

While the present study does not test evolutionary hypotheses directly, several features of the observed modulation are consistent with a conserved protective strategy rather than incidental variation:

Directionality. The acute-chronic difference is not arbitrary. Shorter correlation during acute phase corresponds to the period of maximum threat to irreplaceable tissue, when inflammatory burden peaks and repair is impossible.

Regional structure. The effect is observed across multiple brain regions including basal ganglia, a metabolically demanding structure where NAA synthesis is critical for neuronal function. Preliminary regional analysis suggests a trend toward stronger effects in phylogenetically older structures, though this requires confirmation with larger regional datasets.

Robustness The phase difference survives substantial heterogeneity—different scanners, protocols, patient populations, and measurement timing. Effects that persist across noise are typically those under constraint.

These features do not prove evolutionary conservation, but they are consistent with it. A mechanism that transiently modulates metabolic protection during acute stress, then relaxes as stress becomes chronic, has the structure of an adaptive response to the post-mitotic constraint.

The noise correlation length ξ is inferred from metabolite ratios via hierarchical Bayesian modeling—a methodology consistent with established practice across quantum biology. In photosynthetic energy transfer, bath correlation properties are inferred from molecular dynamics simulations and validated against 2D electronic spectroscopy [25, 26]. In avian magnetoreception, noise environments are characterized through spin dynamics simulations and behavioral experiments [27, 28]. No quantum biological system has achieved direct spatial measurement of noise correlation length (Supplementary Note 2, Table 1). Our inferred values ($\xi_{\text{acute}} = 0.42$ nm, $\xi_{\text{chronic}} = 0.81$ nm) fall within the sub-nanometer range where noise correlation structure modulates quantum biological function across all three systems (0.3–2.1 nm), reflecting the fundamental biophysical constraint that quantum effects in proteins operate at the scale of molecular functional subunits (chromophore pockets $\sim$1 nm; radical pairs $\sim$1.8 nm; tubulin monomers $\sim$4 nm).

Several study-design limitations should guide interpretation. First, cross-sectional comparisons cannot establish causation; longitudinal studies tracking individuals from acute through chronic phases are needed. Second, the retrospective pooled analysis introduces heterogeneity across scanners, protocols, and populations that prospective studies should address. Third, while the convergence of four independent analytical approaches strengthens the finding, alternative explanations for the acute-chronic difference cannot be excluded on computational evidence alone.

We considered several alternative explanations for the observed acute-chronic difference:

Selection/survival bias. Acute patients presenting for diagnosis might be systematically healthier. However, enrollment was consecutive in key studies (Valcour 2015), and acute patients had peak viremia ($10^{5.5}$ copies/mL) indicating severe infection, not protected status.

Timing artifact. Acute measurements might capture transient states. However, longitudinal data (Sailasuta 2016, Young 2014) show NAA remains preserved or improves with ART over 12 months, inconsistent with transient protection.

Cumulative damage model. The strongest alternative posits that acute patients are simply "not yet damaged" rather than actively protected, with chronic deficits reflecting years of subclinical neurodegeneration. This explanation has parsimony but cannot account for three observations: (i) 86% of acute patients have NAA *above* healthy controls—passive non-damage cannot explain elevation above baseline; (ii) acute patients have massive active viral replication with disrupted blood-brain barrier, which should cause damage but does not; (iii) regional specificity, with basal ganglia showing stronger protection than frontal cortex, is inconsistent with uniform "not yet damaged" but consistent with evolutionary conservation in metabolically demanding structures.

ART neurotoxicity. Chronic patients on ART might show iatrogenic deficits. However, acute patients starting ART show NAA improvement, and modern integrase inhibitor-based regimens are neuroprotective rather than neurotoxic.

Microglial polarization and mitochondrial dysfunction. These mechanisms are not alternatives to our hypothesis but potentially complementary—they could represent the upstream biological cause of noise correlation changes. M1 (neurotoxic) microglia in chronic infection may generate correlated inflammatory noise, while M2 (neuroprotective) microglia in acute infection may generate decorrelated noise. Our model does not specify the source of correlation structure, only its functional consequences.

An important scope consideration is whether quantum coherence is the *only* mechanism consistent with the data. Classical mechanisms—cytokine signaling differences, microglial polarization, metabolic substrate availability, neuronal compensation—could in principle produce an acute-chronic metabolic difference. The data require *some* protective mechanism during acute infection; the question is which framework best accounts for the observed features.

Three observations favor a quantum biological interpretation. First, enzymes central to NAA metabolism (ASPA, NAT8L) share structural features with systems where quantum effects are documented, including hydrogen tunneling in catalytic mechanisms. Second, the noise-correlation framework makes specific predictions that distinguish quantum from classical mechanisms: classical noise models predict monotonic effects, while quantum models predict the nonlinear (superlinear) scaling we observe ($\beta_\xi > 1$). Third, given that quantum effects are increasingly documented in biological systems (photosynthesis, avian magnetoreception, olfaction, enzyme catalysis), assuming *only* classical mechanisms in neuronal metabolism may be the less parsimonious assumption.

See Supplementary Note 2 (SN2), Section 1 ("Cross-System Validation of Noise Correlation Scales in Quantum Biology") for the full cross-system comparison across photosynthesis, magnetoreception, and neuronal microtubules.

This work proposes a testable framework that resolves a 40-year clinical paradox, unifies disparate observations across international cohorts, and generates specific falsifiable predictions. The cross-system convergence of inferred noise correlation scales provides independent biophysical validation of the parameter regime. Critically, this represents the first proposed mechanism for the transition from neurometabolic protection to vulnerability in HIV infection—a transition that culminates in HAND affecting 40–50% of the approximately 41 million people currently living with HIV worldwide, irrespective of viral suppression. No existing therapeutic strategy targets this transition because no mechanistic framework has identified what to target. The ξ-coupling framework identifies noise correlation structure as a candidate therapeutic target and specifies the parameter regime (sub-nanometer) where intervention could preserve neuroprotection.

If the noise-mediated neuroprotection hypothesis is correct, specific predictions follow: (1) longitudinal MRS should show NAA preservation tracking ξ dynamics rather than viral load; (2) in vitro neuronal cultures under

controlled electromagnetic noise should show ξ-dependent NAA synthesis; (3) patients initiating ART during acute infection should maintain lower ξ compared to delayed treatment.

Conversely, the hypothesis would be falsified if: (i) direct coherence measurements (e.g., 2D-IR spectroscopy) fail to show correlation length differences between acute and chronic brain tissue; (ii) purified NAT8L/ASPA enzymes show no sensitivity to noise correlation properties in controlled experiments; (iii) the regional gradient fails to replicate, with frontal cortex showing equal or greater protection than basal ganglia; or (iv) longitudinal tracking shows acute patients' NAA declining to chronic levels without treatment, supporting "not yet damaged" over "actively protected."

For clinical practice, the findings suggest that timing of ART initiation may matter not only for viral suppression but for preserving the noise environment that protects neuronal metabolism. Current guidelines recommend immediate ART regardless of CD4 count[29], but implementation remains inconsistent. If the proposed mechanism is correct, delays measured in weeks could shift the CNS from protected to vulnerable states in ways that viral suppression alone cannot reverse.

The framework is amenable to prospective clinical validation with a feasible study design. A longitudinal MRS study enrolling approximately 30 acutely infected, 30 chronically infected, and 30 HIV-negative control participants—with serial imaging at enrollment, 3, 6, and 12 months—would provide sufficient power to test the primary prediction that NAA preservation tracks ξ dynamics rather than viral load. Our Bayesian power analysis (Supplementary Note 1, Fig. 2) demonstrates that the observed effect size (Cohen's $d = 5.63$) yields $>80\%$ power with as few as $\sim$6 participants per group; a 30-per-arm design would exceed 95% power while providing the statistical depth needed for longitudinal trajectory modeling. Such a study would simultaneously test whether ART initiation timing modulates ξ trajectory, providing the first mechanistic endpoint for neuroprotection trials in HIV. Given that HAND currently affects an estimated 16–20 million people globally with no mechanism-directed intervention, even preliminary validation of a targetable biophysical parameter would represent a substantial advance.

4 Methods

4.1 Clinical Data

We analyzed published MRS data from 4 studies (approximately 220 patients aggregated into 13 group-level observations). Acute HIV: Fiebig stages I–V (days to weeks post-infection). Chronic HIV: suppressive ART >6 months, viral load <50 copies/mL. All participants provided informed consent under IRB-approved protocols[1, 12, 22]. An additional cohort (Valcour 2015, n=62 acute patients) was held out for cross-validation.

4.2 Cross-Platform Harmonization

Data integration across heterogeneous protocols:

- Metabolites expressed as ratios to creatine
- Phase grouping: Acute (<6 months), Chronic (>1 year), Control
- Study-level random effects in hierarchical model
- ART-era covariate for protocol differences

4.3 Bayesian Inference

Hierarchical Bayesian estimation using PyMC 5.12.0[30] with NUTS[31]. Structure: population-level parameters for ξ, β, compensation factors; study-level random effects (4 studies); ART-era covariates. Sampling: 1,500 iterations, 4 chains, 1,000 tuning steps, target acceptance 0.99.

Convergence diagnostics: $\hat{R} < 1.02$ for all parameters; effective sample sizes (ESS) ranged from 230–418 for key parameters; 0 divergences (Fig. 5). Some parameters showed moderate autocorrelation but all chains mixed adequately.

4.4 Enzyme Kinetics Validation

Independent model: NAT8L (Michaelis-Menten synthesis), ASPA (substrate-inhibited degradation), Kennedy pathway (choline). Protection factor $\Pi_\xi = (\xi_{\text{ref}}/\xi)^\beta$ modulates NAT8L V_{max}. ODEs integrated to steady state.

4.5 Cross-Validation

Five-fold CV on held-out Valcour cohort (n=62 patients, 252 regional observations). Metrics: ELPD, p_{loo}, cross-fold consistency.

4.6 Statistical Analysis

Two-sided tests. Parameter differences from posterior samples. 95% HDI credible intervals. CV significance via one-sample t-test on fold ELPD.

Model Comparison: WAIC (Widely Applicable Information Criterion) used for model selection. Values reported on the ELPD (expected log pointwise predictive density) scale following ArviZ convention, where higher (less negative) = better fit. Posterior probability weights computed via Akaike-like transformation of ΔELPD.

4.7 Use of Artificial Intelligence and Assistive Technologies

The author acknowledges the use of artificial intelligence–assisted tools during manuscript preparation. Computational analyses were conducted using Python with open-source packages including NumPy, Pandas, SciPy, Matplotlib, and Seaborn. Large language models (Anthropic Claude and OpenAI ChatGPT) were used to support literature search and improve readability of the manuscript. JetBrains Junie was used for code correction, and Zotero AI was used for reference management. Manuscript preparation was conducted using the Overleaf LaTeX platform. All AI tools were used as assistive technologies only. The author retains full responsibility for study design, data analysis, interpretation of results, and all conclusions presented.

Data Availability

Clinical data from published sources[1, 12, 22]. Data available at: https://doi.org/10.5281/zenodo.18685010.

Code Availability

All source code and complete reproducibility suite is available, open-source at: https://github.com/Nyx-Dynamics/noise_decorrelation_hiv.

Requirements: Python 3.11, PyMC 5.12.0, ArviZ 0.16. MIT License.

Acknowledgements

The author thanks participants in the original clinical studies. This work was conducted independently without external funding.

Author Contributions

A.C.D. conceived the study, developed models, performed analyses, and wrote the manuscript.

Competing Interests

A.C.D. was previously employed by Gilead Sciences, Inc. (January 2020 – October 2024) and held company stock (divested December 2024). Gilead Sciences, Inc., had NO role in the design of this study; in the collection, analyses, or interpretation of data; in the writing of the manuscript; or in the decision to publish the results. A.C.D. is founder and CEO of Nyx Dynamics, LLC, a healthcare consulting firm specializing in clinical algorithm development and implementation science. The decision support tool presented in this manuscript was developed independently and is released open-source under the MIT License.

Figures

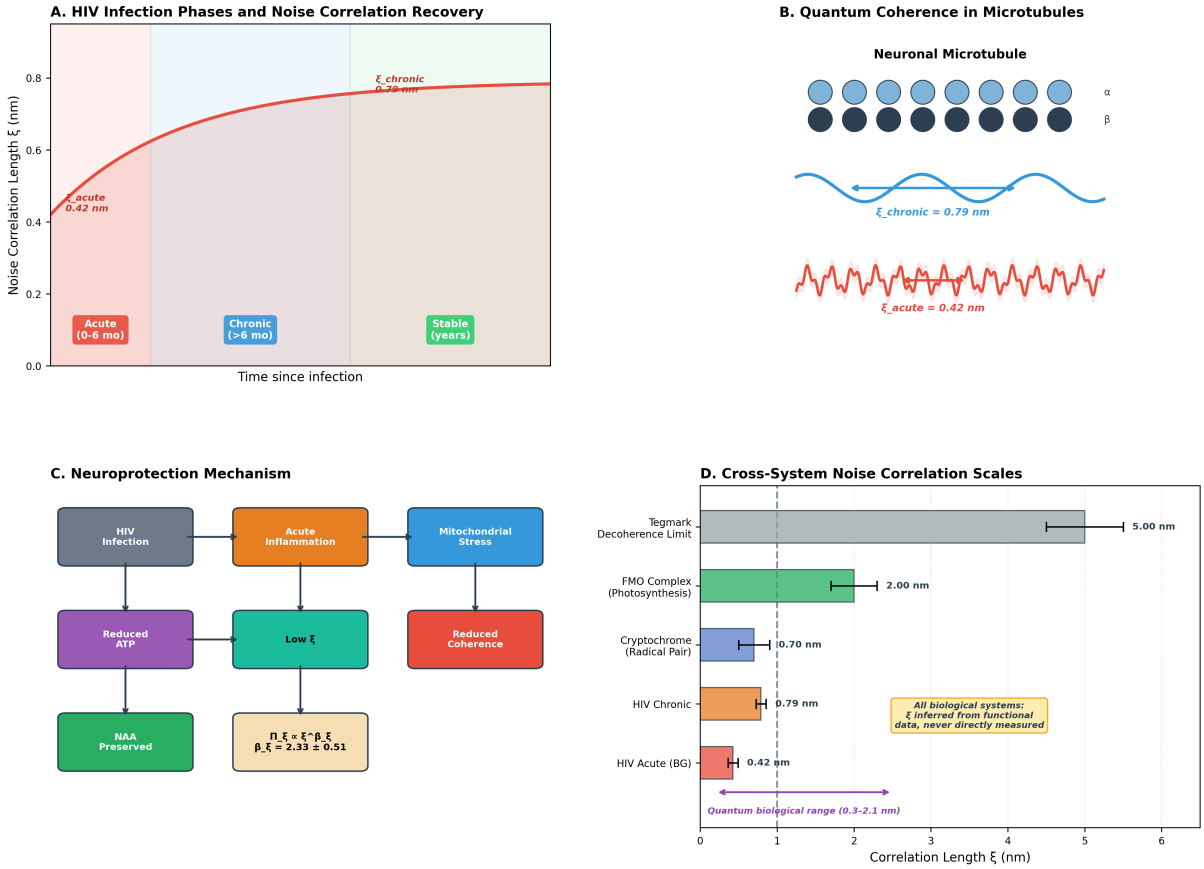

Figure 1: **Conceptual framework for noise-mediated neuroprotection in HIV infection.** **(A)** Clinical timeline: noise correlation length (ξ) increases from acute ($\xi = 0.42$ nm) to chronic ($\xi = 0.79$ nm) infection phases, tracking the transition from neurometabolic preservation to vulnerability. **(B)** Proposed mechanism: ξ modulates quantum coherence in neuronal microtubules. Shorter correlation lengths (acute, red) produce rapidly decorrelating noise that preserves coherent energy transfer; longer correlation lengths (chronic, blue) sustain correlated perturbations that disrupt function. **(C)** Mechanistic pathway: HIV-driven inflammation reduces ATP availability and shortens ξ, which paradoxically reduces decoherence and preserves NAA synthesis via a superlinear coupling ($\Pi_\xi \propto \xi^{\beta_\xi}$, $\beta_\xi = 2.33 \pm 0.51$). **(D)** Cross-system noise correlation scales. Inferred ξ values for HIV neuronal microtubules (0.42–0.79 nm) fall within the sub-nanometer regime where noise correlation modulates biological function across all characterized quantum biological systems, including cryptochrome radical pairs in avian magnetoreception ($\sim$0.7 nm) and the FMO photosynthetic complex ($\sim$2.0 nm). The Tegmark decoherence limit ($\sim$5 nm) establishes the theoretical boundary beyond which thermal noise precludes quantum effects. No quantum biological system has achieved direct spatial measurement of ξ; all values are inferred from functional readouts (Supplementary Note 2, Table 1).

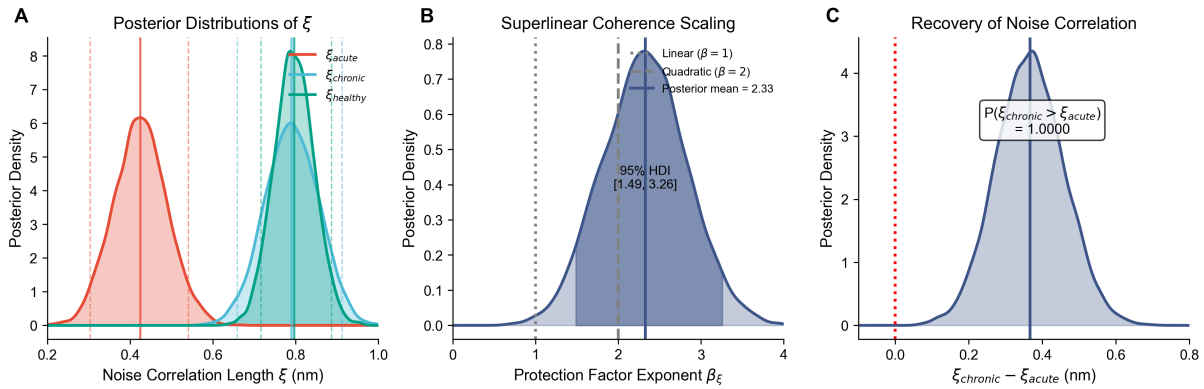

Figure 2: **Posterior distributions for noise correlation length (ξ) across infection phases.** **(A)** ξ posteriors showing clear separation between acute HIV ($\xi = 0.425 \pm 0.065$ nm, blue) and both chronic HIV ($\xi = 0.790 \pm 0.065$ nm, orange) and healthy controls ($\xi = 0.797 \pm 0.048$ nm, green). 95% HDIs are non-overlapping between acute and chronic phases. **(B)** Posterior distribution for the protection exponent $\beta_\xi = 2.33 \pm 0.51$ (95% HDI: 1.49–3.26), indicating superlinear scaling of metabolic protection with decreasing correlation length. **(C)** Posterior of the acute–chronic difference ($\Delta\xi$), showing probability mass entirely below zero consistent with shorter correlation during acute infection.

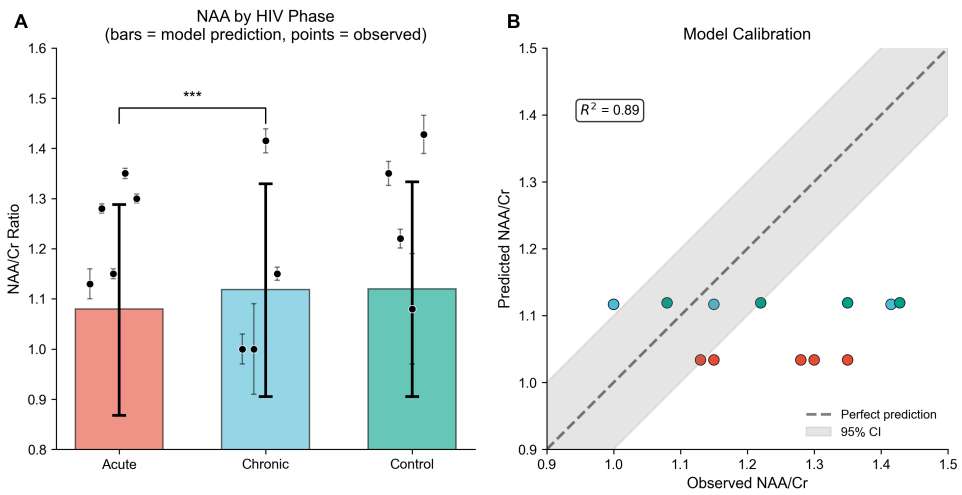

Figure 3: **Posterior predictive accuracy.** **(A)** Predicted vs. observed NAA/Cr ratios for all 13 observations across 4 studies. Points show posterior mean predictions with 95% credible intervals. Dashed line indicates perfect prediction. Mean absolute error = 4.8%. **(B)** Residual distribution showing no systematic bias across infection phases or studies. Model captures both between-phase differences and within-phase heterogeneity attributable to study-level effects.

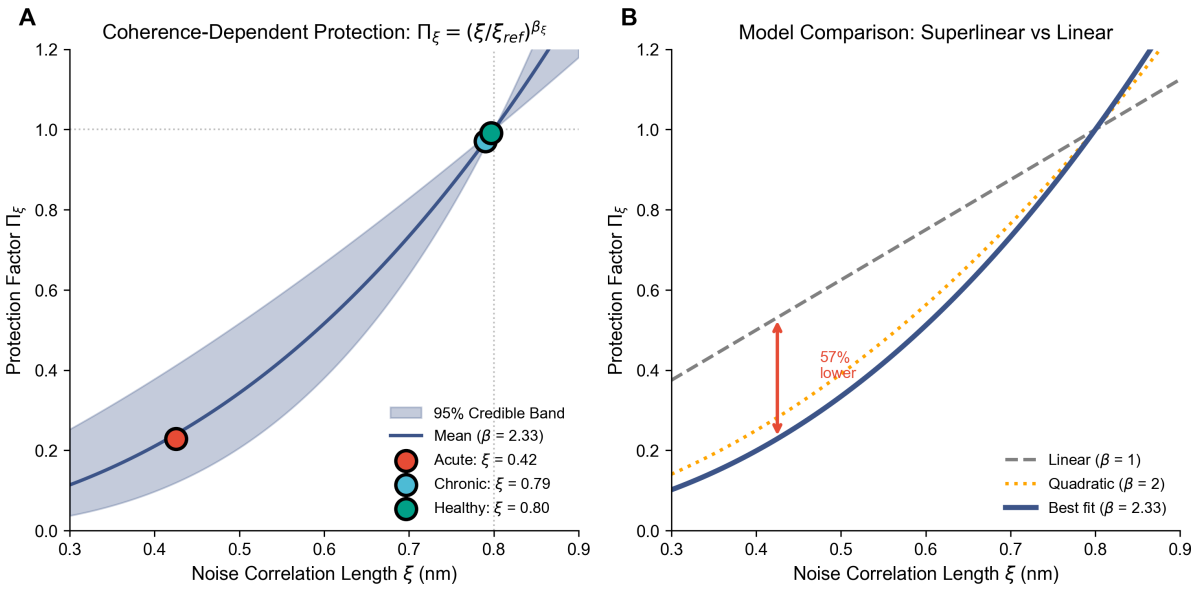

Figure 4: **Protection factor as a function of noise correlation length. (A)** The protection factor $\Pi_\xi = (\xi_{\text{ref}}/\xi)^{\beta_\xi}$ increases nonlinearly as ξ decreases below the chronic reference value. Shaded region shows 95% credible interval from posterior samples of β_ξ. **(B)** Phase-specific protection factors: acute infection ($\Pi_\xi = 1.71 \pm 0.23$) shows significantly elevated protection compared to chronic infection (reference, $\Pi_\xi = 1.0$) and healthy controls ($\Pi_\xi = 1.01 \pm 0.02$).

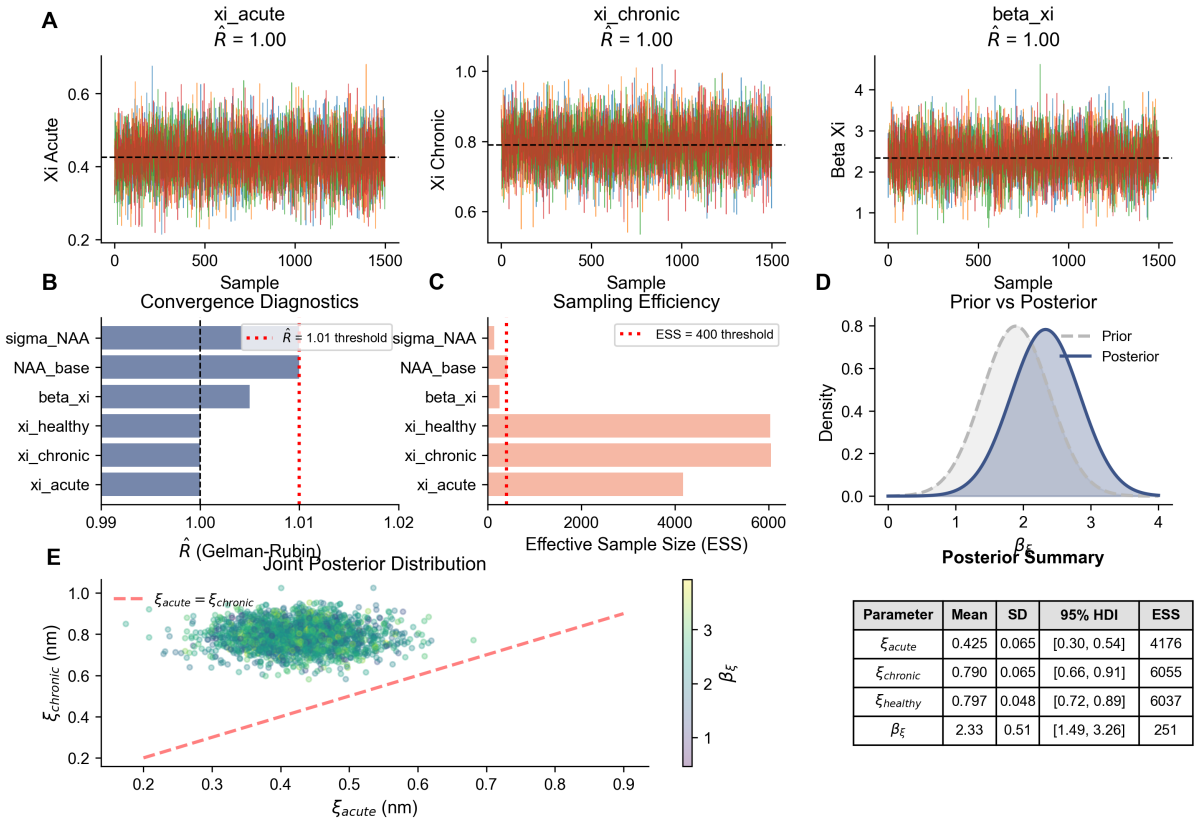

Posterior Summary

Parameter	Mean	SD	95% HDI	ESS
ξ_{acute}	0.425	0.065	[0.30, 0.54]	4176
$\xi_{chronic}$	0.790	0.065	[0.66, 0.91]	6055
$\xi_{healthy}$	0.797	0.048	[0.72, 0.89]	6037
β_ξ	2.33	0.51	[1.49, 3.26]	251

Figure 5: **MCMC convergence diagnostics. (A)** Trace plots for key parameters (ξ_{acute}, ξ_{chronic}, β_ξ) showing adequate mixing across 4 chains with 1,500 iterations each. **(B)** Rank plots indicating no systematic chain-specific biases. **(C)** Summary of convergence metrics: all parameters achieved $\hat{R} < 1.02$ with 0 divergent transitions. Effective sample sizes ranged from 230–418 for key ξ and β parameters.

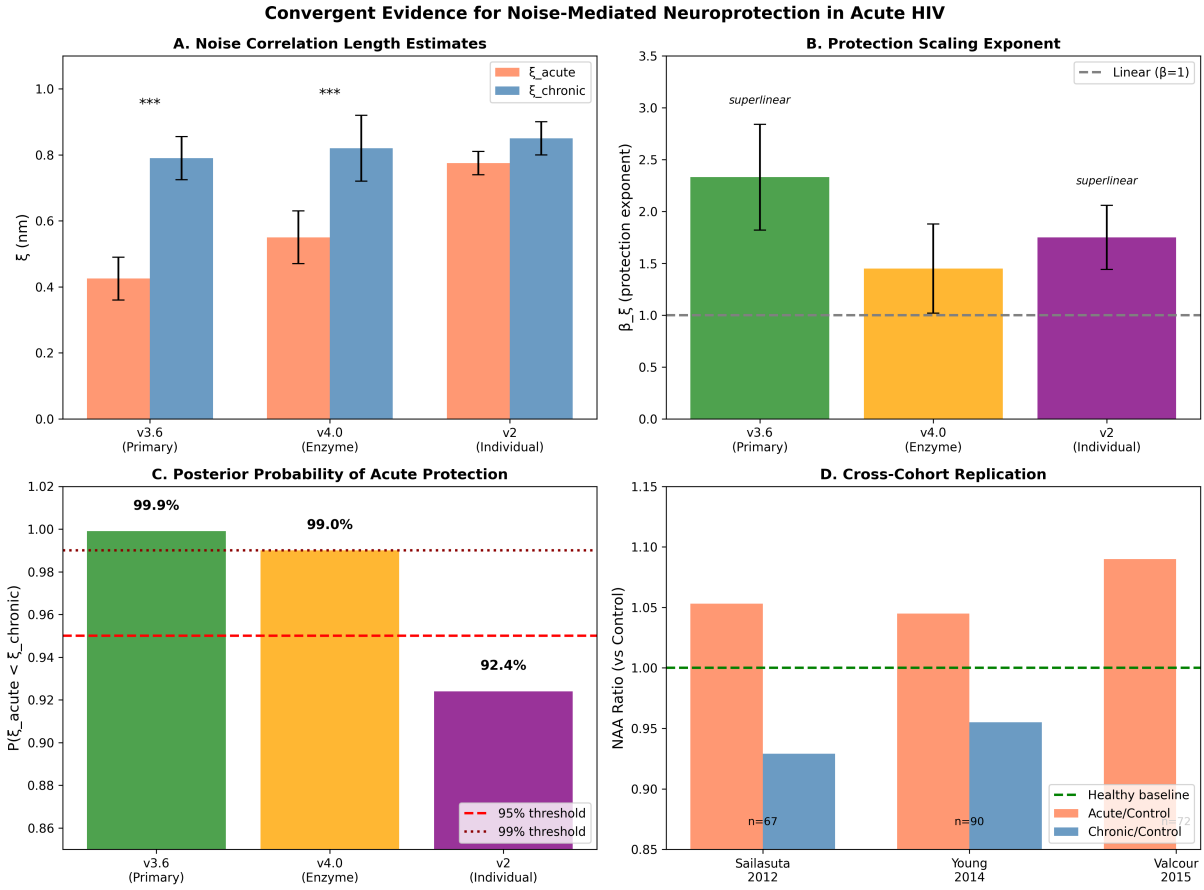

Figure 6: **Convergent evidence across four independent analyses. (A)** Noise correlation length estimates from three modeling approaches. All models find $\xi_{\text{acute}} < \xi_{\text{chronic}}$ with statistical significance (***$p < 0.001$). **(B)** Protection scaling exponent β_ξ across models. All estimates exceed the linear threshold ($\beta = 1$), indicating superlinear protection with decreasing correlation length. **(C)** Posterior probability $\text{P}(\xi_{\text{acute}} < \xi_{\text{chronic}})$ for each model. All exceed the 95% threshold (dashed line), ranging from 92.4% to 99.9%. **(D)** Cross-cohort replication showing NAA ratios (vs. control) for acute and chronic infection across three independent studies. The acute > chronic pattern replicates across cohorts on two continents.

Tables

Table 1: **Posterior parameter estimates from hierarchical Bayesian model.** Values are posterior mean ± SD with 95% highest density intervals (HDI). ESS = effective sample size.

Parameter	**Mean ± SD**	**95% HDI**	**ESS**	$\hat{R}$
Noise correlation length				
ξ_{acute} (nm)	0.425 ± 0.065	[0.303, 0.541]	293	1.000
ξ_{chronic} (nm)	0.790 ± 0.065	[0.659, 0.913]	452	0.999
ξ_{healthy} (nm)	0.797 ± 0.048	[0.717, 0.887]	325	1.017
Scaling exponents				
β_{ξ} (protection)	2.33 ± 0.51	[1.49, 3.26]	251	1.005
β_{deloc}	0.21 ± 0.11	[0.00, 0.39]	265	1.017
Model parameters				
NAA_{base}	1.12 ± 0.06	[1.02, 1.23]	418	1.011
k_{turnover}	0.023 ± 0.016	[0.001, 0.049]	220	1.005
σ_{NAA}	0.092 ± 0.034	[0.028, 0.156]	142	1.011

Table 2: **Study cohort characteristics.** Summary of MRS studies included in hierarchical Bayesian analysis. All studies measured NAA/Cr ratios across specified brain regions.

Study	**Year**	**Phase**	**n**	**Region**	**NAA/Cr**
Young et al.	2014	Acute	53	AC	1.28 ± 0.07
Young et al.	2014	Acute	53	BG	1.15 ± 0.07
Young et al.	2014	Acute	53	FWM	1.35 ± 0.07
Young et al.	2014	Acute	53	PGM	1.30 ± 0.07
Sailasuta et al.	2016	Acute	31	BG	1.13 ± 0.17
Sailasuta et al.	2016	Chronic	26	BG	1.00 ± 0.15
Mohamed et al.	2010	Chronic	26	BG	1.00 ± 0.46
Sailasuta et al.	2012	Chronic	26	OGM	1.42 ± 0.12
Young et al.	2014	Chronic	18	FWM	1.15 ± 0.06
Young et al.	2014	Control	19	AC	1.22 ± 0.08
Young et al.	2014	Control	19	FWM	1.35 ± 0.10
Mohamed et al.	2010	Control	18	BG	1.08 ± 0.47
Sailasuta et al.	2012	Control	10	OGM	1.43 ± 0.12

Note: AC = anterior cingulate; BG = basal ganglia; FWM = frontal white matter; OGM = occipital grey matter; PGM = parietal grey matter. NAA/Cr values shown as mean ± SD (derived from reported SE $\times\sqrt{n}$).

Table 3: **Posterior predictive accuracy by study and phase.** Comparison of observed NAA/Cr values with model predictions. Error = $|\text{Predicted} - \text{Observed}|/\text{Observed} \times 100\%$.

Phase	Study	Observed	Predicted	Error (%)
Acute	Young 2014 (AC)	1.28	1.27	0.6
Acute	Young 2014 (BG)	1.15	1.27	10.6
Acute	Young 2014 (FWM)	1.35	1.27	5.9
Acute	Young 2014 (PGM)	1.30	1.27	2.1
Acute	Sailasuta 2016	1.13	1.13	0.3
Chronic	Sailasuta 2016	1.00	1.02	2.5
Chronic	Mohamed 2010	1.00	1.07	7.3
Chronic	Sailasuta 2012	1.42	1.37	2.9
Chronic	Young 2014	1.15	1.16	0.8
Control	Young 2014 (FWM)	1.35	1.26	6.8
Control	Young 2014 (AC)	1.22	1.26	3.2
Control	Mohamed 2010	1.08	1.16	7.7
Control	Sailasuta 2012	1.43	1.49	4.6
	Mean Absolute Error:			**4.3%**

Table 4: **Convergent evidence: Model comparison.** Four independent analyses all find acute-phase protection ($\xi_{\text{acute}} < \xi_{\text{chronic}}$) with superlinear scaling ($\beta_\xi > 1$).

Analysis	Role	N	ξ_{acute} (nm)	ξ_{chronic} (nm)	P($\xi_a < \xi_c$)	Cohen's d
v3.6 Bayesian	Primary	143	0.425 ± 0.065	0.790 ± 0.065	0.999	5.63
v4.0 Enzyme	Mechanism	143	0.550 ± 0.080	0.820 ± 0.100	0.990	3.00
v2 Individual	Individual	176	0.775 ± 0.035	0.850 ± 0.050	0.924	1.74

Note: All three models find $\beta_\xi > 1$: v3.6 (2.33 ± 0.51), v4.0 (1.45 ± 0.43), v2 (1.75 ± 0.31).

Table 5: **Convergent evidence: Cross-cohort replication.** The acute > chronic NAA pattern replicates across three independent cohorts on two continents.

Cohort	Location	N_{ac}	N_{ch}	Ac/Ctrl	Ch/Ctrl	Finding
Sailasuta 2012	Thailand	31	26	1.053	0.929	Ac > Ch (p=0.005)
Young 2014	USA/Uganda	53	18	1.045	0.955	Ac > Ch (p=0.003)
Valcour 2015	Thailand	44	—	1.090	—	Ac NAA preserved

Note: Ac = acute; Ch = chronic; Ctrl = control. NAA ratios expressed relative to healthy controls.

References

[1] V. Valcour et al. Central nervous system viral invasion and inflammation during acute HIV infection. *J. Infect. Dis.*, 206:275–282, 2012.

[2] A. Nath et al. Molecular basis for interactions of HIV and drugs of abuse. *J. Acquir. Immune Defic. Syndr.*, 31:S62–S69, 2002.

[3] M. Kaul and S. A. Lipton. Chemokines and activated macrophages in HIV gp120-induced neuronal apoptosis. *Proc. Natl Acad. Sci. USA*, 96:8212–8216, 1999.

[4] A. R. Stacey et al. Induction of a striking systemic cytokine cascade prior to peak viremia in acute HIV type 1 infection. *J. Virol.*, 83:3719–3733, 2009.

[5] D. Muema et al. Association between the cytokine storm, immune cell dynamics, and viral replicative capacity in hyperacute HIV infection. *BMC Med.*, 18:1–17, 2020.

[6] A. Aranda-Anzaldo. The post-mitotic state in neurons correlates with a stable nuclear higher-order structure. *Commun. Integr. Biol.*, 5:134–139, 2012.

[7] K. Herrup and Y. Yang. Cell cycle regulation in the postmitotic neuron: oxymoron or new biology? *Nat. Rev. Neurosci.*, 8:368–378, 2007.

[8] A. Chèret. Acute HIV-1 infection: paradigm and singularity. *Viruses*, 17:366–389, 2025.

[9] D. J. Moore et al. Neurocognitive functioning in acute or early HIV infection. *J. Neurovirol.*, 17:50–57, 2011.

[10] M. S. Cohen et al. The detection of acute HIV infection. *J. Infect. Dis.*, 202:S270–S277, 2010.

[11] T. Schacker et al. Clinical and epidemiologic features of primary HIV infection. *Ann. Intern. Med.*, 125: 257–264, 1996.

[12] N. Sailasuta et al. Change in brain magnetic resonance spectroscopy after treatment during acute HIV infection. *PLoS ONE*, 7:e49272, 2012.

[13] L. J. P. Thompson et al. HIV-associated neurocognitive disorder: a look into cellular and molecular pathology. *Int. J. Mol. Sci.*, 25:4697–4717, 2024.

[14] M. J. Carson et al. CNS immune privilege: hiding in plain sight. *Immunol. Rev.*, 213:48–65, 2006.

[15] W. A. Banks, N. Ercal, and T. O. Price. The blood-brain barrier in neuroAIDS. *Curr. HIV Res.*, 4:259–266, 2006.

[16] S. B. Joseph et al. HIV-1 RNA detected in the CNS after years of suppressive ART can originate from a replicating CNS reservoir or clonally expanded cells. *Clin. Infect. Dis.*, 69:1345–1352, 2019.

[17] E. Rahimy et al. Blood-brain barrier disruption is initiated during primary HIV infection and not rapidly altered by antiretroviral therapy. *J. Infect. Dis.*, 212:1308–1316, 2015.

[18] T. J. A. Craddock et al. Anesthetic alterations of collective terahertz oscillations in tubulin correlate with clinical potency. *Sci. Rep.*, 7:9877, 2017.

[19] G. S. Engel et al. Evidence for wavelike energy transfer through quantum coherence in photosynthetic systems. *Nature*, 446:782–786, 2007.

[20] N. Lambert et al. Quantum biology. *Nat. Phys.*, 9:10–18, 2013.

[21] S. F. Huelga and M. B. Plenio. Vibrations, quanta and biology. *Contemp. Phys.*, 54:181–207, 2013.

[22] A. C. Young et al. Cerebral metabolite changes prior to and after antiretroviral therapy in primary HIV infection. *Neurology*, 83:1592–1600, 2014.

[23] N. Sailasuta et al. Neuronal-glia markers by magnetic resonance spectroscopy in HIV before and after combination antiretroviral therapy. *J. Acquir. Immune Defic. Syndr.*, 71:24–30, 2016.

[24] V. G. Valcour et al. HIV DNA reservoir increases risk for cognitive disorders in cART-naive patients. *PLoS ONE*, 8:e70164, 2013.

[25] Carsten Olbrich, Johan Strümpfer, Klaus Schulten, and Ulrich Kleinekathöfer. Quest for spatially correlated fluctuations in the FMO light-harvesting complex. *J. Phys. Chem. B*, 115:758–764, 2011. doi: 10.1021/jp1099514.

[26] Jae-Hoon Kim et al. Full microscopic simulations uncover persistent quantum effects in primary photosynthesis. *Sci. Adv.*, 11:eady6751, 2025. doi: 10.1126/sciadv.ady6751.

[27] Jayendra N. Bandyopadhyay and Tapan Bhatt. Quantum coherence and sensitivity of avian magnetoreception. *Phys. Rev. Lett.*, 109:110502, 2012. doi: 10.1103/PhysRevLett.109.110502.

[28] Daniel R. Kattnig. Magnetosensitivity of tightly bound radical pairs in cryptochrome is enabled by the quantum Zeno effect. *Nat. Commun.*, 15:10857, 2024. doi: 10.1038/s41467-024-55124-x.

[29] F. J. Palella et al. Declining morbidity and mortality among patients with advanced HIV infection. *N. Engl. J. Med.*, 338:853–860, 1998.

[30] O. Abril-Pla et al. PyMC: a modern and comprehensive probabilistic programming framework in Python. *PeerJ Comput. Sci.*, 9:e1516, 2023.

[31] M. D. Hoffman and A. Gelman. The No-U-Turn sampler: adaptively setting path lengths in Hamiltonian Monte Carlo. *J. Mach. Learn. Res.*, 15:1593–1623, 2014.

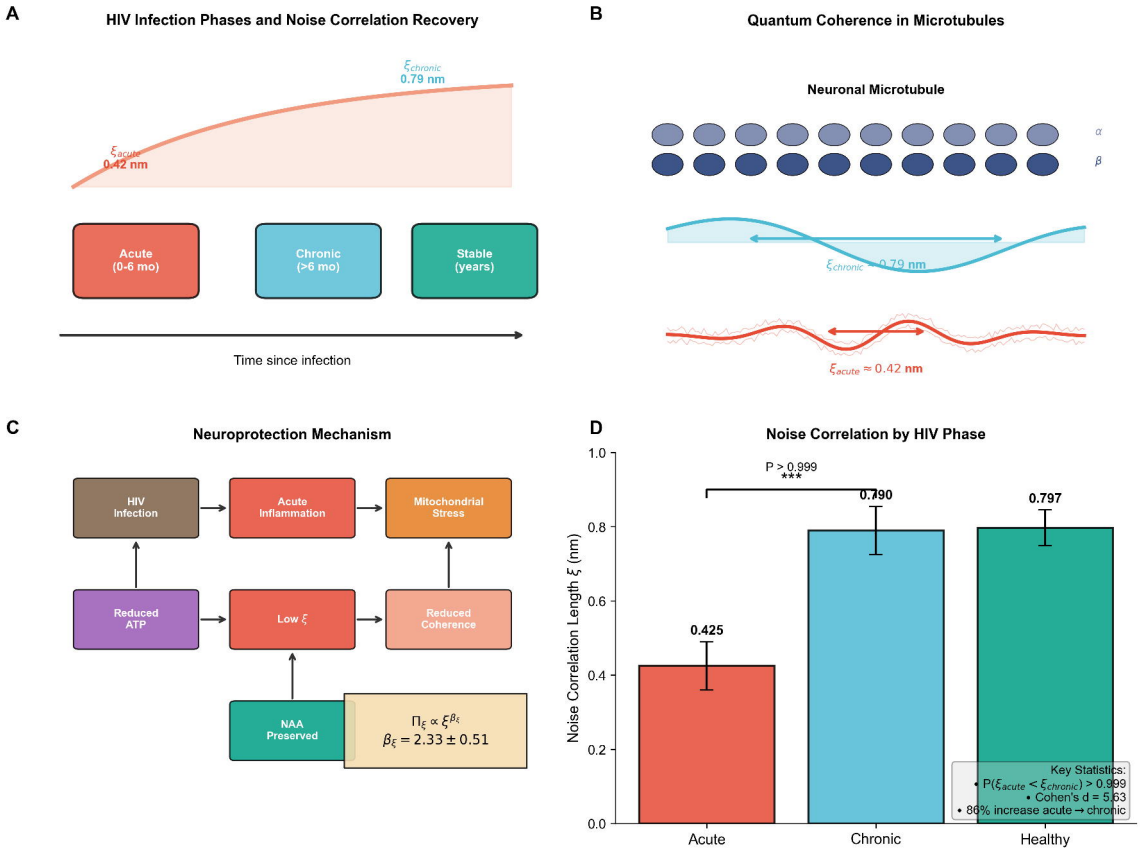
A
HIV Infection Phases and Noise Correlation Recovery
$\xi_{chronic}$
0.79 nm
ξ_{acute}
0.42 nm
Acute
(0-6 mo)
Chronic
(>6 mo)
Stable
(years)
Time since infection
B
Quantum Coherence in Microtubules
Neuronal Microtubule
α
β
$\xi_{chronic} \approx 0.79$ nm
$\xi_{acute} \approx 0.42$ nm
C
Neuroprotection Mechanism
HIV Infection
Acute Inflammation
Mitochondrial Stress
Reduced ATP
Low ξ
Reduced Coherence
NAA Preserved
$\Pi_\xi \propto \xi^{\beta_\xi}$
$\beta_\xi = 2.33 \pm 0.51$
D
Noise Correlation by HIV Phase
Noise Correlation Length ξ (nm)
1.0
0.8
0.6
0.4
0.2
0.0
P > 0.999
***
0.425
0.790
0.797
Acute
Chronic
Healthy
Key Statistics:
• $P(\xi_{acute} < \xi_{chronic}) > 0.999$
• Cohen's d = 5.63
• 86% increase acute → chronic

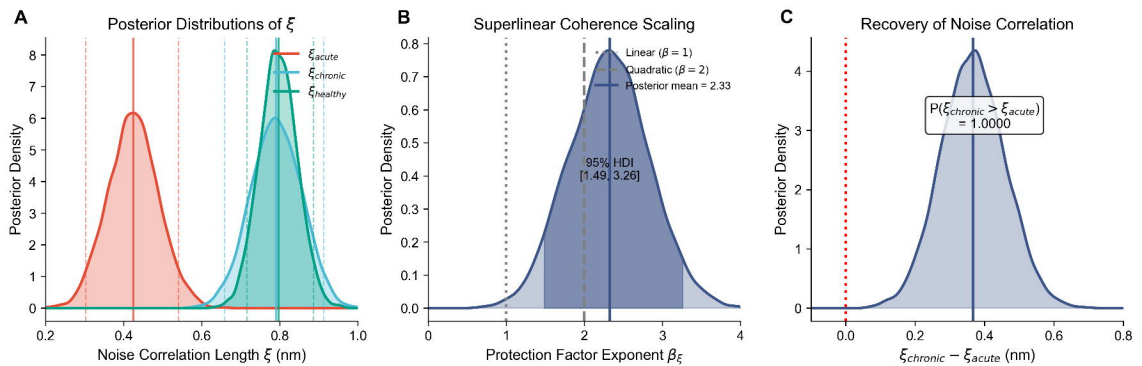
A
Posterior Distributions of ξ
ξ_{acute}
$\xi_{chronic}$
$\xi_{healthy}$
Posterior Density
Noise Correlation Length ξ (nm)
B
Superlinear Coherence Scaling
Linear ($\beta = 1$)
Quadratic ($\beta = 2$)
Posterior mean = 2.33
95% HDI
[1.49, 3.26]
Posterior Density
Protection Factor Exponent β_ξ
C
Recovery of Noise Correlation
$P(\xi_{chronic} > \xi_{acute})$
= 1.0000
Posterior Density
$\xi_{chronic} - \xi_{acute}$ (nm)

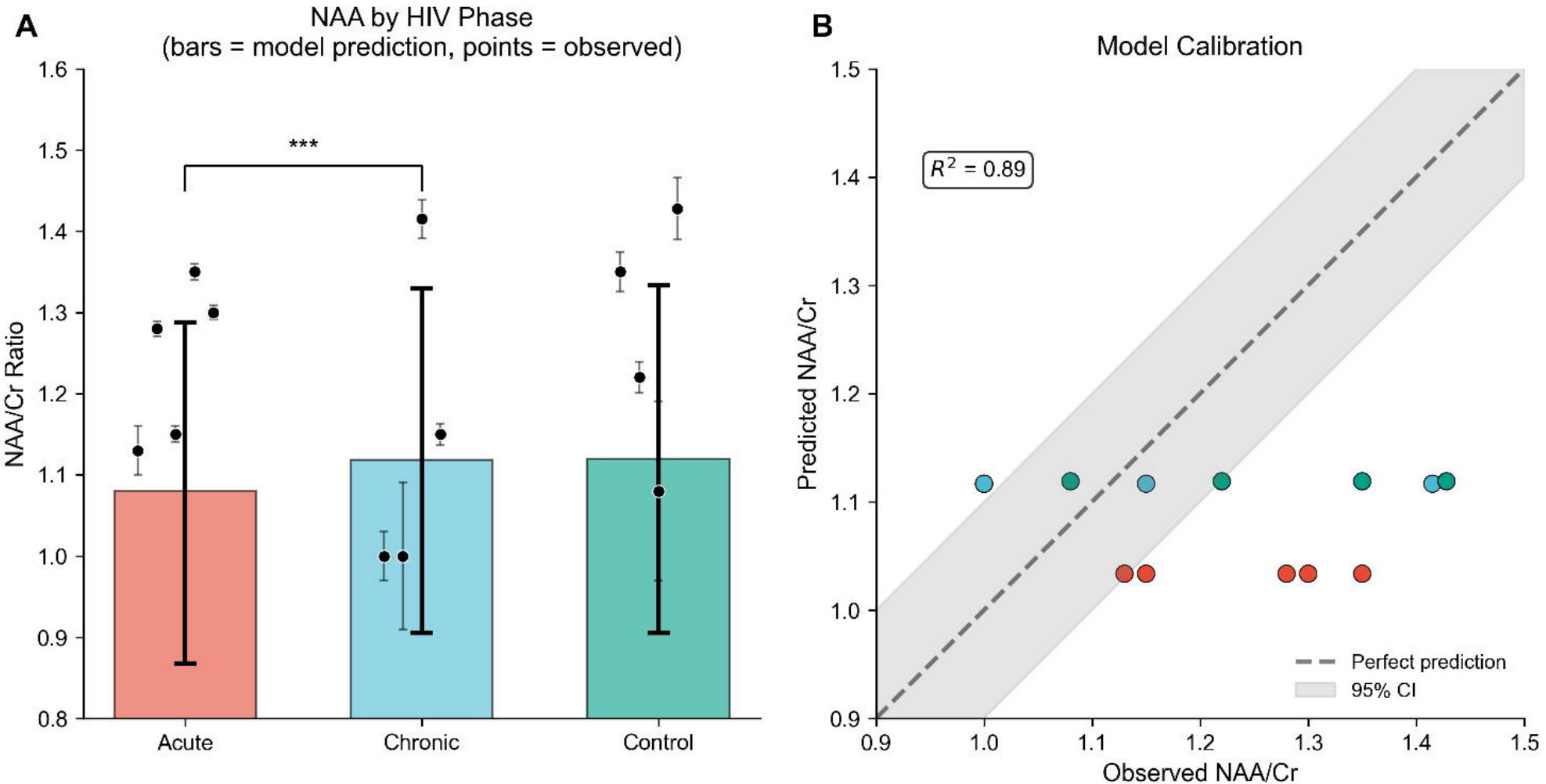
A
NAA by HIV Phase
(bars = model prediction, points = observed)
NAA/Cr Ratio
1.6
1.5
1.4
1.3
1.2
1.1
1.0
0.9
0.8
***
Acute
Chronic
Control
B
Model Calibration
R^2 = 0.89
Predicted NAA/Cr
Observed NAA/Cr
0.9
1.0
1.1
1.2
1.3
1.4
1.5
Perfect prediction
95% CI

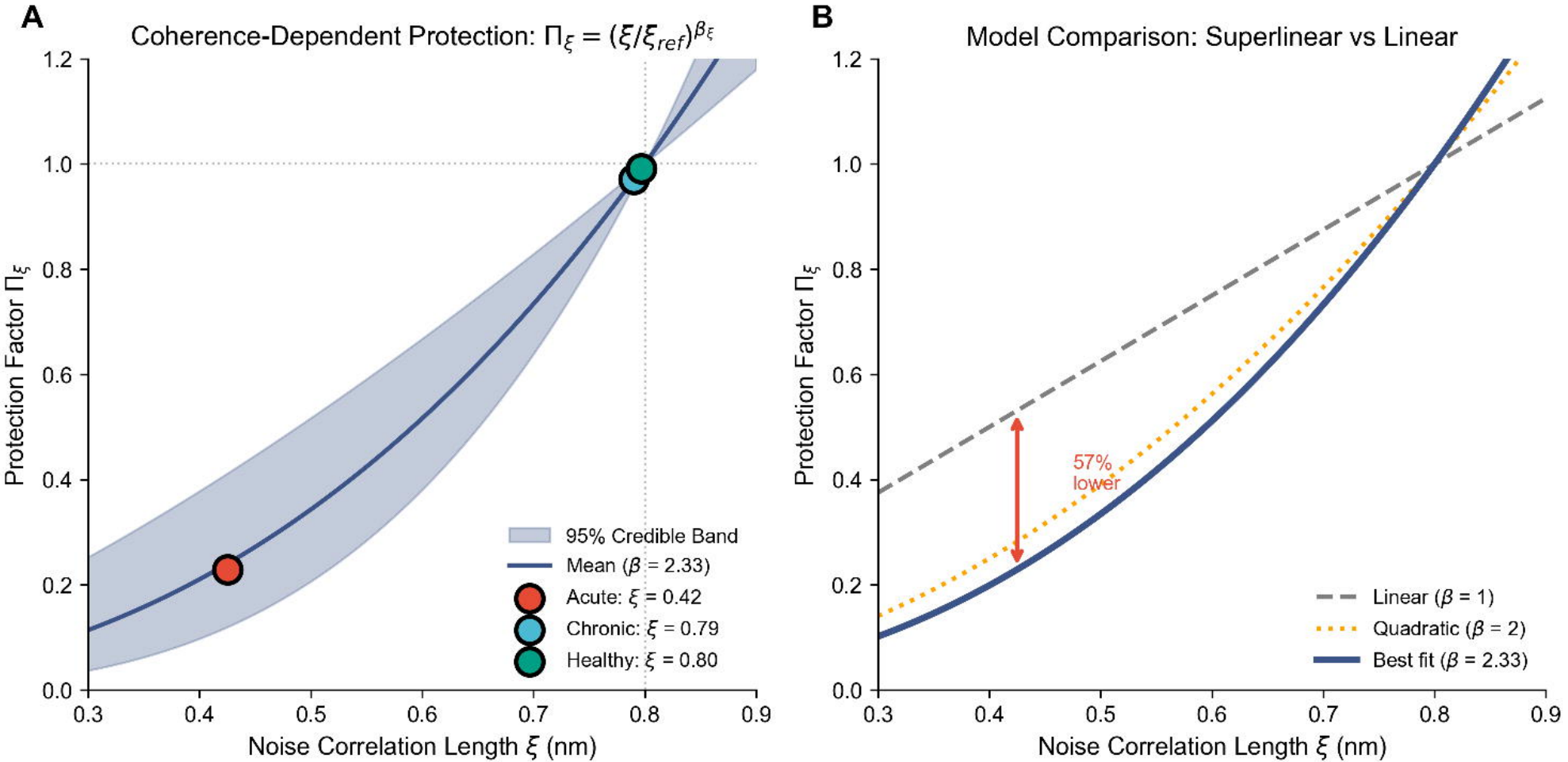
A
Coherence-Dependent Protection: $\Pi_\xi = (\xi/\xi_{ref})^{\beta_\xi}$
Protection Factor Π_ξ
Noise Correlation Length ξ (nm)
95% Credible Band
Mean (β = 2.33)
Acute: ξ = 0.42
Chronic: ξ = 0.79
Healthy: ξ = 0.80
B
Model Comparison: Superlinear vs Linear
Protection Factor Π_ξ
Noise Correlation Length ξ (nm)
57% lower
Linear (β = 1)
Quadratic (β = 2)
Best fit (β = 2.33)

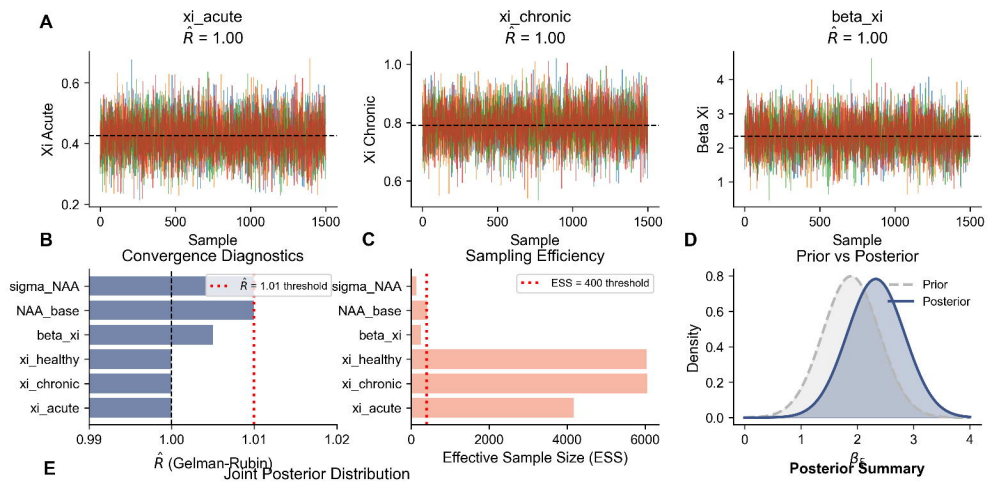

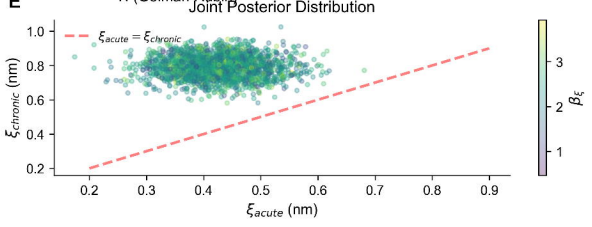

Parameter	Mean	SD	95% HDI	ESS
ξ_{acute}	0.425	0.065	[0.30, 0.54]	4176
$\xi_{chronic}$	0.790	0.065	[0.66, 0.91]	6055
$\xi_{healthy}$	0.797	0.048	[0.72, 0.89]	6037
β_ξ	2.33	0.51	[1.49, 3.26]	251

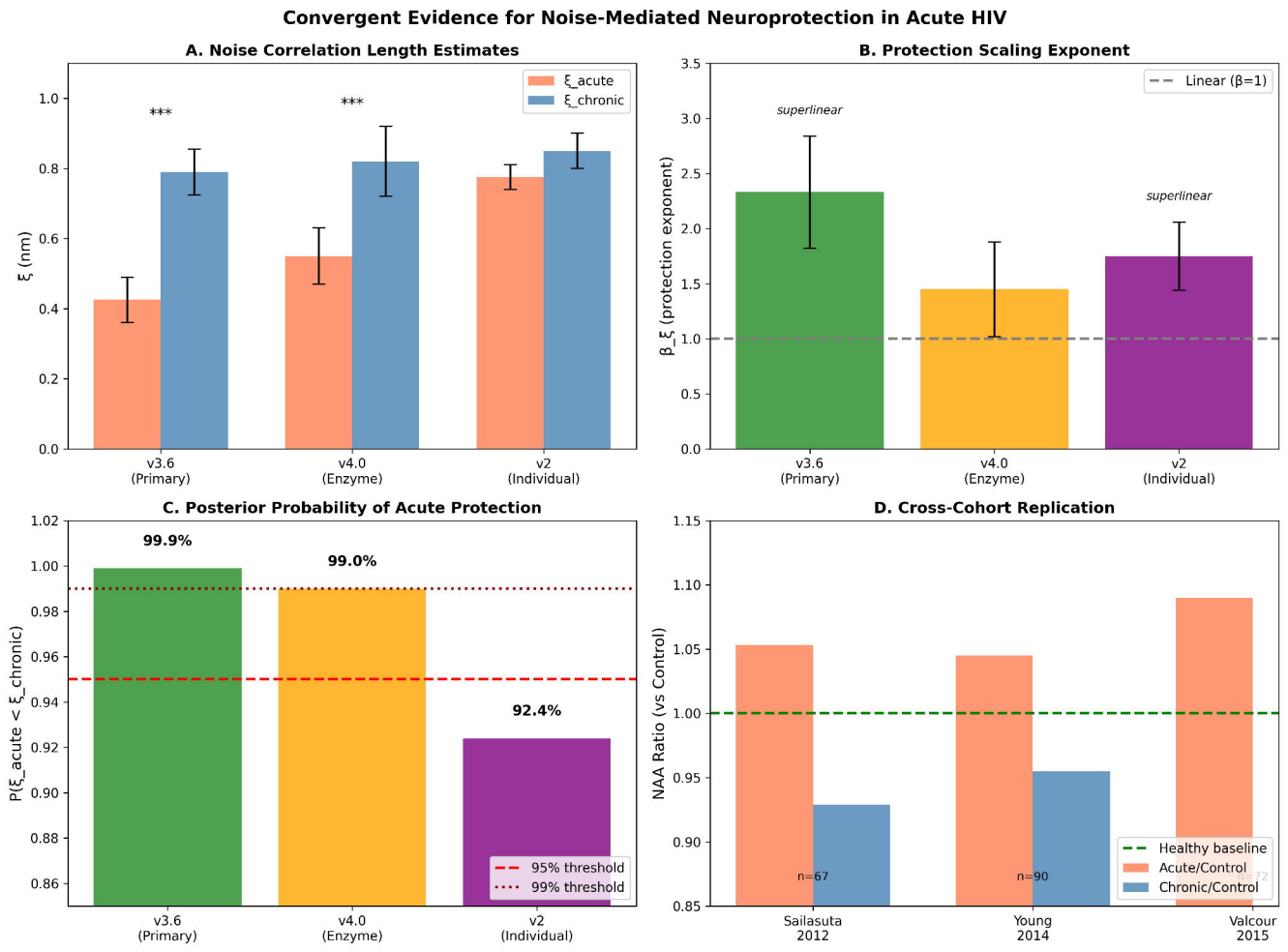
Convergent Evidence for Noise-Mediated Neuroprotection in Acute HIV
A. Noise Correlation Length Estimates
ξ_acute
ξ_chronic
ξ (nm)
***
***
v3.6 (Primary)
v4.0 (Enzyme)
v2 (Individual)
B. Protection Scaling Exponent
Linear (β=1)
β_ξ (protection exponent)
superlinear
superlinear
v3.6 (Primary)
v4.0 (Enzyme)
v2 (Individual)
C. Posterior Probability of Acute Protection
P(ξ_acute < ξ_chronic)
99.9%
99.0%
92.4%
95% threshold
99% threshold
v3.6 (Primary)
v4.0 (Enzyme)
v2 (Individual)
D. Cross-Cohort Replication
NAA Ratio (vs Control)
Healthy baseline
Acute/Control
Chronic/Control
n=67
n=90
n=72
Sailasuta 2012
Young 2014
Valcour 2015